

See discussions, stats, and author profiles for this publication at: <https://www.researchgate.net/publication/247696645>

Plastic Deformation of Semicrystalline Polyethylene by X-ray Scattering: Comparison with Atomistic Simulations

ARTICLE in MACROMOLECULES · JUNE 2013

Impact Factor: 5.8 · DOI: 10.1021/ma4005007

CITATIONS

7

READS

159

6 AUTHORS, INCLUDING:



Justin Che

Stony Brook University

14 PUBLICATIONS 67 CITATIONS

[SEE PROFILE](#)



Rebecca Locker

ExxonMobil

9 PUBLICATIONS 119 CITATIONS

[SEE PROFILE](#)



Benjamin S Hsiao

Stony Brook University

571 PUBLICATIONS 20,554 CITATIONS

[SEE PROFILE](#)



Andy H. Tsou

ExxonMobil

63 PUBLICATIONS 1,402 CITATIONS

[SEE PROFILE](#)

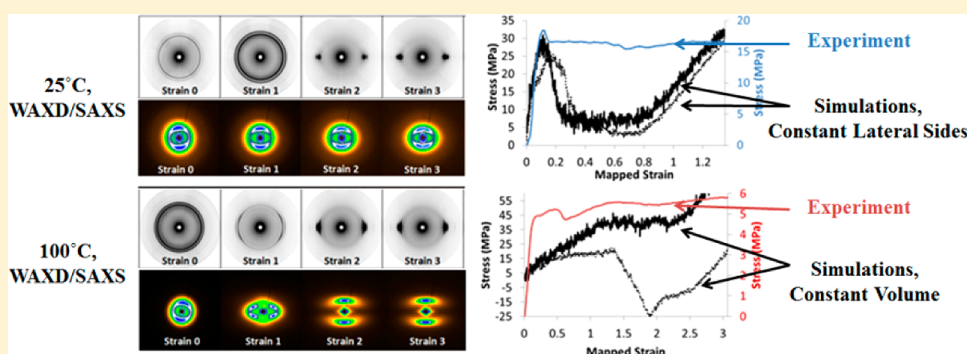
Plastic Deformation of Semicrystalline Polyethylene by X-ray Scattering: Comparison with Atomistic Simulations

Justin Che,^{†,*} C. Rebecca Locker,[‡] Sanghun Lee,[§] Gregory C. Rutledge,[§] Benjamin S. Hsiao,[†] and Andy H. Tsou[‡]

[†]Department of Chemistry, Stony Brook University, Stony Brook, New York 11794-3400, United States

[‡]ExxonMobil Research and Engineering Co., 1545 Rt. 22E, Annandale, New Jersey 08801, United States

[§]Department of Chemical Engineering, Massachusetts Institute of Technology, 77 Massachusetts Avenue, Cambridge, Massachusetts 02139, United States



ABSTRACT: Plastic deformation of uniaxially oriented polyethylene (PE) fiber has been examined by small and wide angle synchrotron X-ray scattering. Morphology changes of the lamellar stack with deformation beyond yielding have been characterized and quantified. Atomistic simulations of tensile deformation of the lamellar stack in the longitudinal direction compare favorably to the experimentally observed morphological changes in the PE fiber. Experimental deformations at 100 °C exhibit responses comparable to those observed by simulation of deformation with constant total volume at 77 °C and a strain rate of $5 \times 10^6 \text{ s}^{-1}$. Experimental deformations of the PE fiber at 25 °C were found to be comparable to simulated tensile deformation with constant lateral dimensions at 77 °C and a strain rate of $5 \times 10^7 \text{ s}^{-1}$. Cavitation in the interlamellar region was found experimentally in the PE fiber deforming at room temperature as predicted by simulation with constant lateral dimensions at the higher strain rate. Melting, recrystallization, and removal of entanglements observed in the PE fiber deformation at 100 °C agree with the simulation results of a constant volume deformation at the slower strain rate. The ability to define the deformation behavior of PE at room and at high temperatures through simulation offers unique opportunities to examine how the interlamellar amorphous topology affects PE deformation.

INTRODUCTION

While it is widely speculated that the strength and mechanical deformation mechanisms of polyethylene (PE) derive from the microscopic topology of the noncrystalline regions in the semicrystalline solid, it is difficult to probe this mainly amorphous region directly through experiment. By combining Raman spectroscopy, differential scanning calorimetry (DSC), and X-ray measurements, the mechanical properties were proposed to be directly correlated with an intermediate phase that links the phases between the crystallites.^{1–5} Data from experiments such as in situ uniaxial tensile deformation small-angle X-ray scattering (SAXS)^{6–9} and other X-ray diffraction studies^{10–15} led to proposed deformation mechanisms of crystallographic slip and mechanical melting, respectively, in the crystalline regions. However, the interpretation of deformation in the amorphous phase is model dependent and amorphous phase contributions to the deformation of a

semicrystalline polymer cannot be quantified directly. Molecular-level simulations of a semicrystalline model (SM) with fully thermalized and deformable crystalline and amorphous components have been conducted to determine the deformation mechanisms of a stacked lamellar unit cell under two deformation modes and strain rates of semicrystalline PE at 350 K.¹⁶ An interphase Monte Carlo (IMC) molecular simulation methodology¹⁷ was applied to create initial configurations for the SM model with proper treatment of chain connectivity and packing density. These configurations were then subjected to molecular dynamics (MD) simulations to explore the temporal evolution of the combined noncrystalline/crystalline system in tensile deformation with large strains. The yielding and plastic

Received: March 13, 2013

Revised: June 7, 2013

Published: June 20, 2013



flow mechanisms were found to be sensitive to the deformation mode and deformation rate. This simulation approach provides experimentally inaccessible insight into how the amorphous region within the semicrystalline solid deforms plastically. In order for the simulation results to be interpreted in the context of real polyethylene deformation scenarios, the mechanical properties and deformation mechanisms identified in these molecular simulations must be validated by comparison to experimental deformation of model materials. While several experimental X-ray scattering studies have probed the *in situ* deformation of PE in the linear elastic regime,^{7–9,18} deformation beyond yielding is required to understand the plastic deformation mechanisms identified in the simulations. To this end, a tensile deformation X-ray scattering study was conducted on a PE fiber with uniaxially aligned stacked lamellar morphology beyond yielding to plastic flow at a constant strain rate and for two temperatures. The small and wide angle scattering data were analyzed to examine morphological changes and orientation in the noncrystalline and crystalline phases in order to establish the deformation mechanisms of polyethylene fibers and to compare the experimental observations with the simulation results.

Two main yielding mechanisms were identified in the simulations of the SM model. Fast deformations and deformations with constant lateral sides were found to yield through cavitation. Slow deformations where the simulation cell was kept at a constant volume resulted in yielding through crystallographic slip. This molecular level SM model is used as a probing tool to identify mechanism(s) for plastic deformation and to understand the stress origins in the semicrystalline lamellar morphology. This SM model acts as a mechanical “microscope” for examining the effects of amorphous topology on plastic deformation. In order to validate the model and to define the bounds of interpretation, a cognate experimental system is essential. In this study, tensile deformation of a model HDPE (high density polyethylene) uniaxially oriented fiber was followed and examined by synchrotron X-ray scattering. The experimental deformation results were compared to simulation findings to validate the simulation protocol, to assess any limitations, if present, and to relate simulation conditions of a given deformation mechanism to corresponding experimental conditions.

EXPERIMENTAL SECTION

Sample Preparation. Linear polyethylene or HDPE, with M_n of 15,400 and M_w of 122,000, with an entanglement molecular weight of 860, is obtained from ExxonMobil Chemical Company. HDPE fibers were prepared using a Rosand RH7 Capillary Rheometer (Malvern Instruments) at a low pull rate of 0.6 m/min to form 1-mm thick monofilament with uniaxially oriented stacked lamellae. To repair any potential defects and to ensure uniaxial alignment, these fibers were stretched using a tensile machine at 1 mm/min to 50% elongation and then relaxed back to 0% while clamping in place for thermal annealing at 80 °C for 1 h. SAXS and WAXD were performed afterward on the fibers to confirm uniaxial symmetry without any microvoids.

X-ray Scattering. Synchrotron X-ray measurements were carried out at the X27C beamline in the National Synchrotron Light Source (NSLS), Brookhaven National Laboratory (BNL). The X-ray wavelength was set at 1.371 Å. Two types of X-ray measurements were performed: wide-angle X-ray diffraction (WAXD) and small-angle X-ray scattering (SAXS). Two-dimensional (2D) WAXD and SAXS patterns were acquired using a MAR-CCD detector. The typical image acquisition time for each scan was 1 min. Al_2O_3 and silver behenate standards were used to calibrate the scattering angle in WAXD and SAXS, respectively. The sample-to-detector distances for

WAXD and SAXS were 133.7 mm and 1783 mm, respectively. X-ray measurements for all samples were taken under the same conditions. All scattering/diffraction signals were corrected for beam fluctuations and background scattering. X-ray scattering data analysis was performed using the software Polar (Stony Brook Technology and Applied Research, Stony Brook, NY). The sample length used in this study was 30 mm. A tensile stretching device that could deliver symmetric sample deformation was used. Structural changes in the sample were monitored by X-ray illuminating the same sample position throughout deformation. The samples were deformed at 25 and 100 °C at a rate of 10 mm/min. Time-resolved WAXD/SAXS patterns and stress/strain values during deformation were recorded simultaneously. The stress is an engineering stress as defined with load divided by the original cross section. The strain is defined as the displacement of the two clamps divided by the original length.

Scattering Data Analysis. For WAXD analysis, quantitative evaluations of crystal mass fractions were determined from the corrected WAXD patterns. The corrected WAXD pattern contains contributions from both the unoriented isotropic and the oriented anisotropic crystalline and amorphous domains. The isotropic and anisotropic contributions in these patterns can be obtained by deconvoluting the corrected WAXD patterns into these separate contributions using the Polar software. The isotropic contribution consists of unoriented amorphous and unoriented crystalline components. The anisotropic contribution consists of the oriented amorphous and oriented crystalline components.

$$I(\text{total}) = I(\text{isotropic}) + I(\text{anisotropic}) \quad (1)$$

$$\begin{aligned} I(\text{isotropic}) &= I(\text{unoriented amorphous}) \\ &+ I(\text{unoriented crystalline}) \end{aligned} \quad (2)$$

$$I(\text{anisotropic}) = I(\text{oriented amorphous}) + I(\text{oriented crystalline}) \quad (3)$$

The integrated intensities of the isotropic and anisotropic contributions were obtained and a two-dimensional peak-fit software was applied to fit all the observed crystal peaks and the amorphous halo. The crystallinity was quantitatively determined by taking the ratio of the integrated crystal peak area (both unoriented and oriented components) by the total integrated peak area. The P_2 orientation factors of the polymer chains along the fibril axis (c -axis) were calculated using the Hermans' orientation function:

$$P_2 = 0.5(3\langle \cos^2 \varphi \rangle - 1) \quad (4)$$

where φ is the angle between the chain axis and the reference axis, and $\langle \cos^2 \varphi \rangle$ is the averaging over all φ given by:

$$\langle \cos^2 \varphi \rangle = \frac{\int_0^{\pi/2} I(\varphi) \cos^2 \varphi \sin \varphi \, d\varphi}{\int_0^{\pi/2} I(\varphi) \sin \varphi \, d\varphi} \quad (5)$$

Since no crystal reflections along the (001) diffraction plane can be observed from the WAXD patterns, an indirect method described by Wilchinsky¹⁹ and Desper et al.²⁰ was used to determine the fibril axis orientation. Using a combination of two or more diffraction planes containing the c -axis, which are the $(hk0)$ planes, the crystallites' orientation with respect to the filament axis can be calculated. In this study, the combination of the (110) and (200) planes were used.

For SAXS analysis, the integrated SAXS pattern was first cleaned up with a Lorentz correction. Afterward, the long period (L) was obtained from the inverse of the scattering vector, s , at the peak maximum. The thicknesses of the crystalline and amorphous layers can be determined from analyzing the combined WAXD and SAXS results using a simple calculation. The crystalline layer thickness ($\langle T \rangle$) is calculated from the product of the crystallinity and the long period. The amorphous layer thickness ($\langle t \rangle$) is then obtained from the difference of the long period and the crystalline layer thickness.

For a more in-depth SAXS analysis, an additional two-phase stacking model, which is adopted from Hermans,²¹ Stribeck,²²

Ruland,²³ and Burger,²⁴ was applied to the experimentally obtained one-dimensional integrated raw SAXS intensities. The stacking model considers a two-phase lamellar system with their planar interfaces oriented parallel to each other.²¹

The intensity distribution through an infinite stack height of lamellae in the one-dimensional reciprocal space ($I_{1D}(s)$) is given by:

$$I_{1D}(s) = \frac{f}{s^4} \operatorname{Re}\left\{ \frac{(1 - H_1(s))(1 - H_2(s))}{1 - H_1(s)H_2(s)} \right\} \quad (6)$$

where s is the scattering vector in reciprocal space [$s = 2(\sin \theta)/\lambda$, θ is the Bragg angle, λ is the wavelength], f is a proportionality constant, $\operatorname{Re}\{\}$ takes the real part of the complex number, and $H_1(s)$ and $H_2(s)$ are the Fourier transforms of the thickness distributions of the two phases. A Gaussian function was chosen as the thickness distributions of the two phases and can be given as

$$H_1(s) = \exp(2\pi i \langle T \rangle s - 2\pi^2 \sigma_T^2 s^2) \quad (7)$$

$$H_2(s) = \exp(2\pi i \langle t \rangle s - 2\pi^2 \sigma_t^2 s^2) \quad (8)$$

where σ_T and σ_t are the standard deviations of the thickness distributions. The long period can then be obtained from the sum of $\langle T \rangle$ and $\langle t \rangle$. An example of the stacking model fitting to the experimental raw SAXS intensity is shown in Figure 1. The structural parameters obtained from stacking model were compared with those obtained from experiments using the simple calculation.

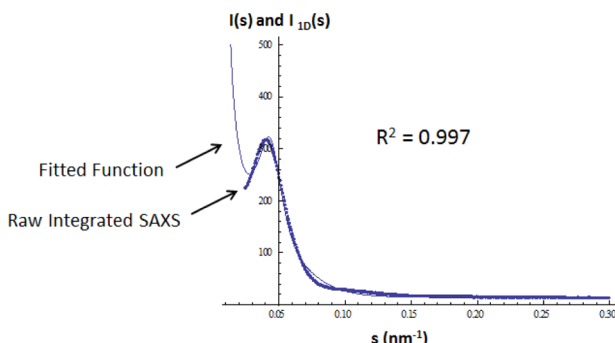


Figure 1. Example of the two-phase stacking model fitting to the experimental integrated raw SAXS intensity.

Simulation Model and Methods. Summaries of the simulation model and protocol are presented here, while details can be found in ref 16. Semicrystalline polyethylene (PE) was modeled using united atom polymer chains, organized into a periodic lamellar stack with alternating crystalline and noncrystalline layers. The stacked lamellae configurations were generated using the Interphase Monte Carlo algorithm,²⁵ and they were subsequently subjected to molecular dynamics simulations with boundary conditions that simulate uniaxial deformation. The stress tensors, velocities and coordinates of each bead were monitored to compute the stress, degree of crystallinity, crystal orientation and local orientation (Hermans' orientation factor) as a function of strain. Two different strain rates and two different modes of deformation were explored.

The individual PE chains were modeled with a united atom model where each bead represents one methylene group with the following potential energy function:¹⁷

$$E = E_b + E_\theta + E_\phi + E_{nb} \quad (9)$$

Here E_b , E_θ , and E_ϕ represent bond stretching, bond bending, and torsional twisting along the chain, respectively. E_{nb} represents pairwise van der Waals interactions between nonbonded beads. The exact forms of each term and the parameters used in this model are discussed in ref 17. This model has been shown to reproduce experimentally observed structure, thermodynamics and dynamics of amorphous PE melts. It has also been shown to capture the melting point and heat of fusion as well as crystal growth kinetics for *n*-alkanes.

Nevertheless, some caution should be exercised when comparing simulation results from this potential energy function directly to PE experiments. The experimentally observed crystal unit cell is orthorhombic with hexagonal symmetry in the *ab*-plane, while the model crystal phase exhibits pseudohexagonal symmetry in the *ab*-plane. This difference is due to the reduced phase space in the model system caused by combining the carbon and attached hydrogen atoms to create a methylene bead, which apparently stabilized the rotator phase with respect to the orthorhombic phase. All-atom simulations of these systems of interest are computationally more expensive, so the united atom system results should be interpreted as a comparable, if not identical system when compared to experiment. It should be noted that the model provides a very good description of *n*-alkanes where the rotator phase is indeed observed experimentally.

A semicrystalline simulation cell with stacked lamellar morphology was created from a single crystal cell using the Interphase Monte Carlo algorithm.²⁵ This protocol is illustrated in Figure 2. Thirty individual

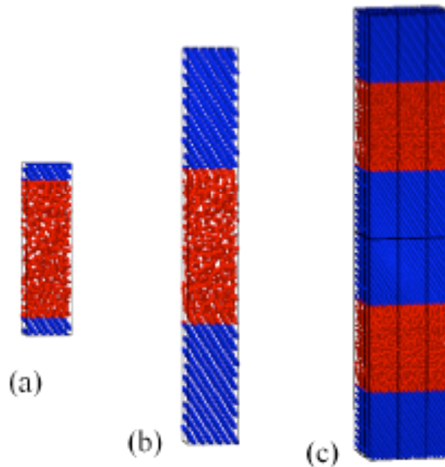


Figure 2. Reproduced from ref 16. Copyright 2011 American Chemical Society. (a) Amorphous topology (red) generated from Interphase Monte Carlo algorithm. (b) Semicrystalline model simulation cell with crystalline beads added at chain ends to give realistic degree of crystallinity, average molecular weight and polydispersity in the model polyethylene system. (c) Visualization of the repeated stacked lamellae resulting from periodic boundary conditions in the Monte Carlo and molecular dynamics simulations.

100-mer chains were packed into the simulation cell with crystalline order, in a lattice of $3 \times 5 \times 50$ unit cells. The lattice was oriented so that the normal to the (201) lattice plane aligned approximately with the *z*-direction of the simulation cell. The cell dimensions were adjusted so the stresses in the chains match the experimentally measured stresses in the crystal phase at atmospheric pressure and $T = 350$ K. In order to create the stacked lamellar morphology within the simulation cell, 6 chains were randomly selected in the center of the cell and cut to form 12 free ends. Beads were then randomly removed from the tails to reach a noncrystalline density of ~ 0.8 g/cm³, slightly higher than that of the amorphous melt extrapolated to 350 K. The first and last 10 beads on each PE chain were held fixed in 3D space to create a crystalline boundary for the interlamellar domain. The system was then randomized under a high temperature (10 000 K) Monte Carlo (MC) simulation with local and global displacements that allow changes in chain connectivity.²⁵ The randomized structure was then annealed with the same MC algorithm and equilibrated at 350 K to identify topologies in the noncrystalline region consistent with the lowest free energy ensemble. The resulting topology in the noncrystalline region consisted of tails (free ends), loops (both ends of the chain are anchored within one crystallite), and tie-chains/bridges (each chain end is anchored in a different crystallite). Finally, the *z*-dimension within the interlamellar domain was adjusted to obtain near-atmospheric pressure of 0.1 MPa over the entire

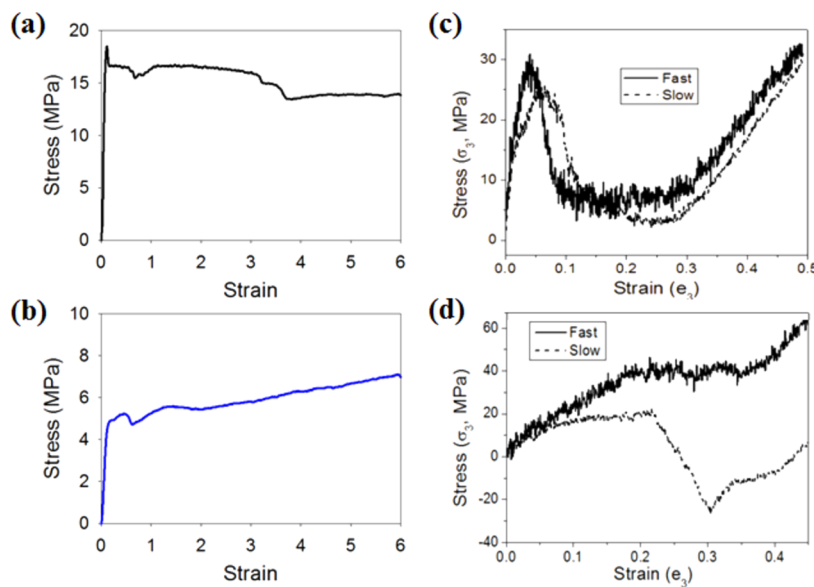


Figure 3. Stress–strain curves for (a) 25 °C experiment, (b) 100 °C experiment, (c) simulation with constant lateral sides, and (d) simulation with constant volume. The simulations in (c) exhibit similar features (yield, plastic deformation, and strain hardening) as the 25 °C experiment, but they tend to occur at lower strains and are more pronounced. Similarly, the slow simulation in part d shows yield, melting, and strain hardening features also seen in the 100 °C experiment, and the simulated features tend to be more pronounced and occur at lower strains.

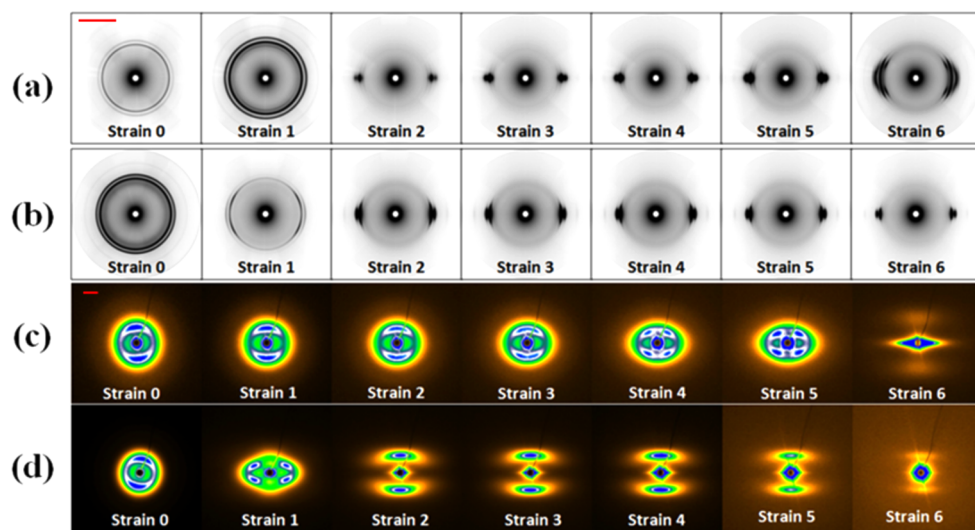


Figure 4. 2D WAXD patterns for the deformation at (a) 25 and (b) 100 °C. 2D SAXS patterns for the deformation at (c) 25 and (d) 100 °C. Scale bars for the WAXD and SAXS patterns are shown as the red line in parts a and c at strain 0. The scale bars for WAXD and SAXS represent 2.35 nm⁻¹ and 0.05 nm⁻¹, respectively.

simulation cell. The resulting amorphous region flanked by the short crystalline domains is shown in Figure 2a. Crystalline ends were then added to each chain in the crystalline domain to yield a simulation cell with 65% crystallinity, number-average molecular weight of 13 100 g/mol and polydispersity index of 1.62. MD simulations in the canonical ensemble with no constraint on the motion of the crystalline beads showed that the constructed configurations were stable over at least 8 ns. A total of 18 independent semicrystalline configurations were generated using this method. The configurations were then subjected to uniaxial tensile deformation in the *z*-direction using two deformation rates (“fast”: 5×10^7 s⁻¹, “slow”: 5×10^6 s⁻¹) and two boundary conditions (constant lateral dimensions, and constant volume where the *x* and *y* cell dimensions shrink with the elongation in the *z*-direction).

RESULTS AND DISCUSSION

X-ray Results During Deformation. Parts a and b of Figure 3 show the experimentally obtained stress–strain curves of HDPE fibers deformed in tension at 25 and 100 °C. Here, the strain value denotes the ratio of the deformed length to its initial length. For example, strain 1 and strain 2 refers to 100% and 200% respectively to its original length of the sample. For deformation at 25 °C, several regions of melting and reconstruction were revealed from strains 0.5 to 3.5 of the stress–strain curve. A significant reduction in stress was observed around strain 3.5 which may be attributed to changes in the microstructure. For deformation at 100 °C, only a region of melting and reconstruction at strain 0.5 was observed, followed by a region of strain-hardening.

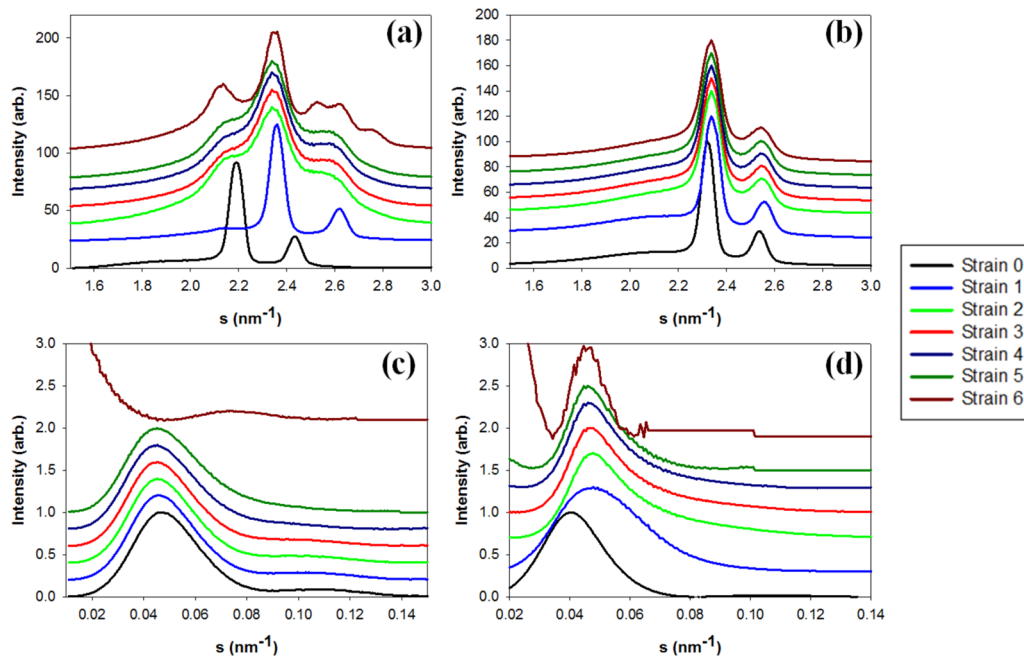


Figure 5. 1D integrated WAXD intensities for the deformation at (a) 25 and (b) 100 °C. 1D integrated SAXS intensities for the deformation at (c) 25 and (d) 100 °C.

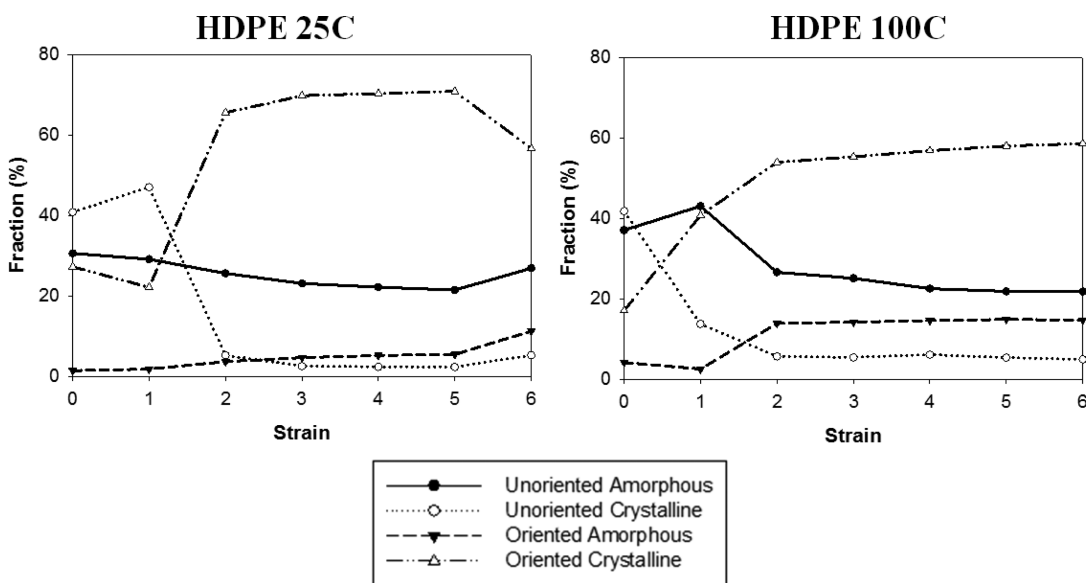


Figure 6. Unoriented isotropic and oriented anisotropic fractions as a function of strain for the deformation of HDPE at 25 and 100 °C.

Figure 4 shows the 2D WAXD and SAXS patterns of HDPE at various strains. The corresponding 1D integrated intensities are shown in Figure 5. Prior to deformation at 25 °C, only the orthorhombic crystal structure can be found in the sample as observed in the integrated WAXD by the presence of the (110) and (200) crystal peaks. Upon deformation to strains above 200% at 25 °C, a mixture of the orthorhombic and monoclinic crystal structures were identified by the presence of additional crystal peaks that coexist and overlaps each other. At strain 6, the peaks of both phases are separated and more apparent, which is due to the increase in the monoclinic phase and a decrease in the orthorhombic phase. On the other hand, only the presence of the orthorhombic structure was observed throughout deformation at 100 °C. From each WAXD pattern, the fractions of unoriented isotropic and oriented anisotropic

contributions as a function of strain were determined and shown in Figure 6. Similar trends were observed at both temperatures. The unoriented fractions of both amorphous and crystalline domains were found to decrease with increasing strain. The conversion from unoriented amorphous domain to oriented amorphous domain was small, whereas significantly more oriented crystalline domains developed during deformation. The conversions from unoriented to oriented crystalline and amorphous fractions were far more pronounced at 100 °C than those changes observed at 25 °C. This is expected since the higher temperature system exhibits faster polymer chain dynamics.

From the WAXD patterns, the P_2 orientation factor of the polymer crystals with respect to the filament axis can be calculated. Figure 7 shows the P_2 orientation factor of the

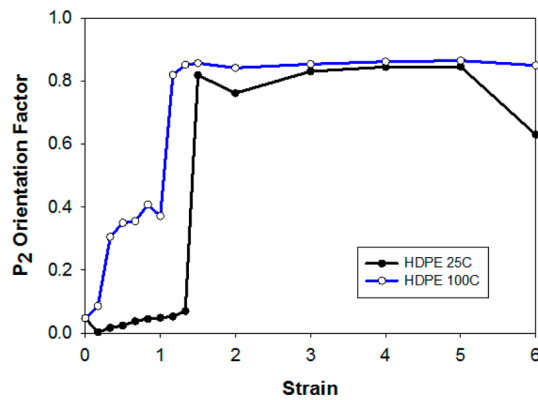


Figure 7. P_2 orientation factor of the polymer crystals with respect to the filament axis as a function of strain for the deformation at 25 and 100 °C.

polymer crystals as a function of strain for the deformation at 25 and 100 °C. The orientation factor prior to deformation was about 0, suggesting random orientation of polyethylene crystals. During deformation, the orientation factor was raised to about 0.9, indicating high alignment of polymer crystals along the stretching direction. The orientation factor was found to be higher during 100 °C deformation than that obtained during deformation at 25 °C.

From the SAXS patterns, prior to deformation at both temperatures, an initial two-point pattern along the meridional axis with an additional ring was observed. Figure 8 shows the polar azimuthal scans at the peak maximum of the lamellar long period at varying strains for the deformation at 25 and 100 °C. The P_2 orientation factors of the lamellar stacks can then be calculated from these polar azimuthal scans of the lamellar long period. The P_2 orientation factors of the lamellar stacks prior to deformation were determined to be 0.30 and 0.32 for the deformation at 25 and 100 °C respectively. This indicated the presence of a very slightly oriented lamellar structure along the meridional axis, which was formed by the uniaxial pulling of the sample during the preparation process.

Figure 9 shows the long period, crystalline layer thickness (represented by $\langle T \rangle$) and amorphous layer thickness (represented by $\langle t \rangle$) as a function of strain for the deformation of HDPE at 25 and 100 °C from (a) the simple calculation method using the experimental WAXD and SAXS results, and (b) the two-phase stacking model fitting. Similar trends in

structural parameters were observed in Figure 9, parts a and b. Upon deformation at 25 °C, the long period was determined to increase with deformation, which arises from the increase in the crystalline layer thickness and the reduction in amorphous layer thickness. Structural rearrangement of the lamellar stacks was observed around strain 3 by the transformation of the two-point pattern into a four-point pattern, representing the presence of chevron morphologies. This is also observed in the polar azimuthal scans with the transformation of the single peak into two peaks at higher strains. During this transformation, changes to the structural morphology of the lamellar stacks were observed as represented by the significant drop in mechanical stress and a very slight reduction in the long period. With the increase in deformation, the four point reflections begin to develop away from the meridional axis and toward the equatorial axis. Intralamellar slippage along with rotation and slight deformation of the lamellar stacks are occurring with the increase in deformation. Further increase in deformation after the four point pattern produces a new two-point pattern along the meridional axis. This new meridional axis reflection has a significantly lower long period, crystalline and amorphous layer thicknesses, which is an indication of the destruction of the original lamellar stacks with the mechanical stretching force.

For the deformation at 100 °C, an initial decrease in the long period, amorphous and crystalline layer thicknesses was observed that can be attributed to the melting and rearrangement of the lamellar stacks around strain 0.5. The transformation into a four-point pattern occurs at much smaller strains at 100 °C (around strain 1) as compared to the deformation at 25 °C (around strain 4), which can also be observed from the polar azimuthal scans. This is consistent with the faster polymer chain dynamics at higher temperatures. After the development of the four-point pattern, the new two-point pattern along the meridional axis was observed in the strain hardening region. An increase in the long period was observed that can be attributed to the increase in the crystalline thickness and decrease in the amorphous thickness. The opposite trend was observed for the deformation at 25 °C, where the new two-point reflection produced a long period that is much lower than the original lamella. Here at 100 °C, the melting and recrystallization create the formation of a more perfect crystal as confirmed with the increase in crystallinity and orientation of crystals with deformation. In addition, the orientation of the lamellar stacks also increased with strain, as shown by

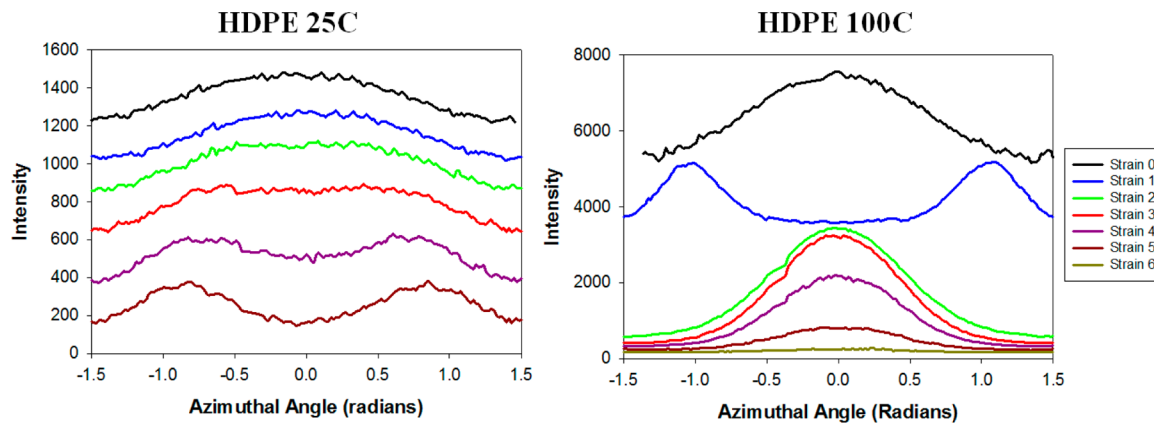


Figure 8. Polar azimuthal scans at the peak maximum of the lamellar long period at varying strains for the deformation at 25 and 100 °C. The intensities were offset to increase clarity.

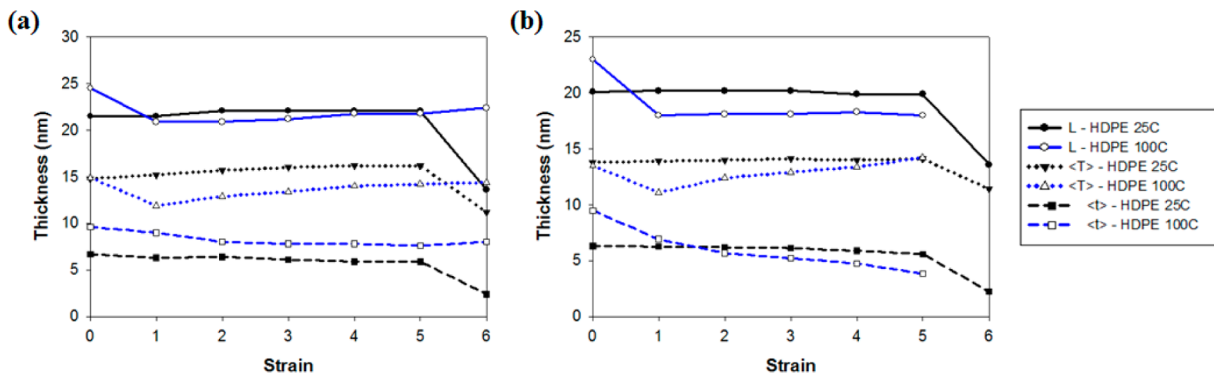


Figure 9. Long period (L), crystalline layer thickness ($\langle T \rangle$), and amorphous layer thickness ($\langle t \rangle$) as a function of strain for the deformation of HDPE at 25 and 100 °C from (a) the simple calculation method using the experimental WAXD and SAXS results, and (b) the two-phase stacking model fitting.

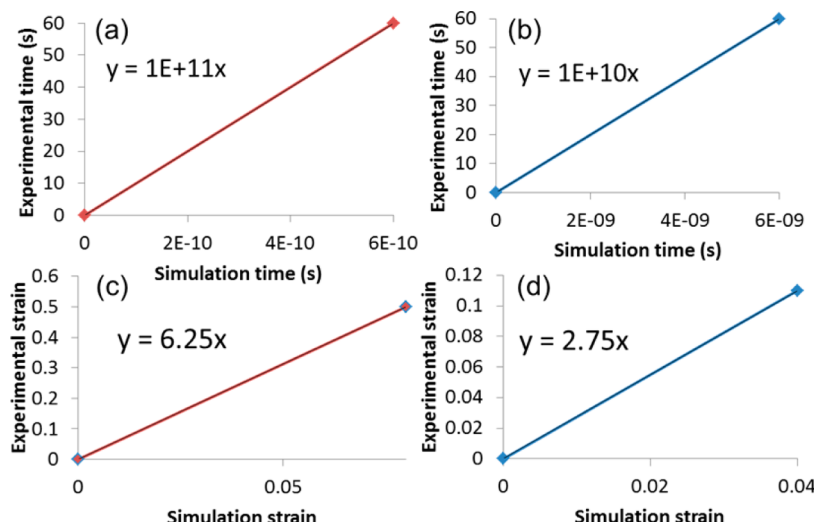


Figure 10. Linear maps between experimental and simulation time and strain. Parts a and c map the constant volume, slow deformation simulation to the 100 °C experiment. Parts b and d map the fixed lateral sides, fast deformation simulation to the 25 °C experiment. Initial points correspond to zero time and strain; final points correspond to time to yield and yield strain for the time and strain maps, respectively.

narrowing of the distribution of the polar azimuthal scans of the lamellar period with the increase in strain. A P_2 value of 0.61 was observed at strain 6 for the lamellar stacks, which is larger than the initial P_2 value of 0.32 prior to deformation.

Furthermore, for the deformation at higher strains for both temperatures, we can observe the presence of equatorial streaks and a diamond shaped morphology around the center of the beam stop in the SAXS patterns, which is attributed to the presence of needle-shaped microvoids between fibrils that are elongated along the fiber axis direction during deformation.

Comparison between Simulation and Experiment. The simulation results presented here are originally reported in ref 16. Although simulations can capture molecular rearrangement details during the deformation, the united atom model used was found to yield a different crystal packing structure. Additionally, a relationship between the modeling boundary conditions and experimental stretching conditions under dynamic, or non-equilibrium, deformation has not been developed. Thus, the simulation time scales and the deformation strain rates do not necessarily form a one-to-one correspondence with experimental time scales and strain rates. Indeed, a qualitative comparison between the stress-strain curves in simulation and experiment, as shown in Figure 3, indicates that while several qualitative features of yield, melting, and strain hardening can

be identified in both simulation and experiment, these features happen at larger strains and later times during the experiment than predicted by the simulations. This can be attributed to the differences in experimental and simulation temperatures, strain rates and degree of initial lamellar alignment. Nonetheless, the qualitative similarities in the stress-strain curves suggest that the united atom model can capture the important deformation features albeit on shorter time scales and at lower strains.

The Eyring model²⁶ has been used in other studies^{27,28} to superpose data collected at different temperatures (T) and strain rates ($\dot{\varepsilon}$) via an activated process, $\dot{\varepsilon} = \dot{\varepsilon}_0 e^{\Delta E - \sigma v^*/k_b T}$, where the activation energy associated with the yield process, ΔE , is modified by the additional work required for the deformation (σv^* , where σ is the applied stress and v^* is the activation volume), and k_b is Boltzmann's constant. This model assumes that the activation energy required for yield is independent of the applied stress, and the pre-exponent, $\dot{\varepsilon}_0$, depends on the temperature and the ensemble of configurations available to surmount the barrier. One could, in principle, use this model to map the simulation stress to experiment. However, the assumptions of constant activation energy and pre-exponential hold over a range of strain rates that is much smaller than the 10^7 s⁻¹ range studied in the current

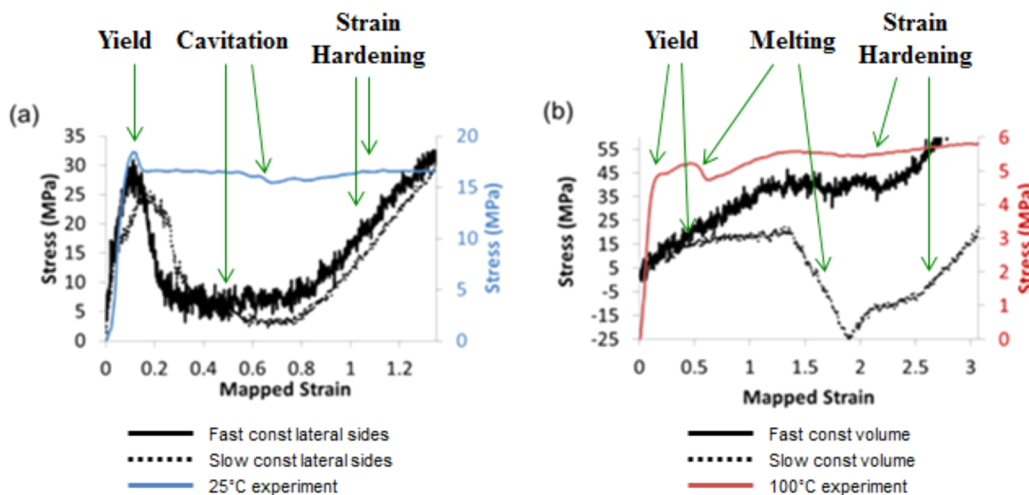


Figure 11. Stress–strain curves for (a) simulation with constant lateral sides (black) and the 25 °C experiment (blue) and (b) simulation with constant volume and the 100 °C experiment (red). The simulation strain is mapped to experimental strain space using the linear maps for time and strain in Figure 8, parts d and c, respectively. The simulations in part a exhibit similar features (yield, plastic deformation, and strain hardening) as the 25 °C experiment, but both postyield softening and subsequent strain hardening are more pronounced. Similarly, the slow simulation in part b shows yield, melting, and strain hardening features also seen in the 100 °C experiment, and the simulated features tend to be more pronounced and occur at higher (mapped) strains.

simulations. A multiple process Eyring model would likely work, but the problem is ill-defined with only two strain rates to define the curve. An alternate approach is to map the phase space of the experimental system onto the simulation phase space by assuming a linear relationship between the two. By choosing a prominent feature in the stress–strain curve (namely, the time and strain at yield) to match the experimental data to the simulations, the data can be compared explicitly. Linear correlation curves in time and strain for the two experimental conditions (25 and 100 °C) and the pertinent simulation conditions are shown in Figure 10.

Detailed comparisons of the stress–strain curves, crystallinity, and evolution of lamella with strain (*vide infra*) suggest that the fast deformation simulation with fixed lateral sides can be mapped to the 25 °C experiment, and that the slow deformation simulation with constant volume can be mapped to the 100 °C experiment. These are the conditions that will be compared and contrasted in the subsequent analysis. Since yielding is the key feature on the stress–strain curve signifying the end of the linear material response, yielding time and strain were chosen as the features to map the simulation time and strain space to the experimental space. The slow simulation with constant volume is mapped to the 100 °C experiment and the fast simulation with constant lateral sides is mapped to the 25 °C experiment. The positive slopes indicate that yield tends to happen faster and at lower strains during the simulation. The fast simulation with constant lateral sides deformed the sample to a mapped strain of $e_m = 1.35$ and the slow simulation with constant volume deformed the sample to a mapped strain of $e_m = 3.07$. Since the HDPE samples were strained to 600% at both experimental temperatures, the comparisons of experimental data and simulation results are restricted to deformations up to a mapped strain of 1.35 and 3.07 for the constant lateral sides and the constant volume simulations, respectively.

The simulation results can be presented in the “experimental space” by plotting all quantities of interest against the mapped strains. The experimental and simulation stresses as a function of mapped strain are plotted in Figure 11. As a result of the mapping, the experimental yield strain at 25 °C is the same

value as that for the fast deformation with fixed lateral sides, shown in Figure 11a. Although the qualitative features are similar, there is no evidence that the fast deformation in Figure 11a more closely follows the low temperature experiment than does the slow deformation simulation. Later comparison of the evolution of crystallinity during deformation will make this similarity between low temperature experiment and fast deformation simulation more apparent. The experimentally measured yield stress of 19 MPa is lower than the simulated yield stress of 29 MPa. This is likely a consequence of the lateral periodic boundary conditions employed in the simulations leading to infinite lamellae in the x - and y -directions which are effectively more resistant to yielding. There is a strain softening and plastic flow after yielding as indicated by simulation and by experiment between $e_m = 0.3$ and 0.8 followed by a strain hardening region beyond $e_m = 0.8$. However, these phenomena are not as pronounced in the experimental data. These observations are likely the result of the differences in morphology between the simulation and experimental systems. The lamellae in the experimental system are only partially aligned initially, with an average Hermans’ orientation factor of 0.3, whereas the perfectly aligned lamellae in the simulation box have a Hermans’ orientation factor of 1.0. Thus, the lamellae in the experimental system are not all subjected to perfect uniaxial deformation. In Figure 11b, it is apparent that the 100 °C experimental stress–strain curve most closely resembles the slow, constant volume deformation simulation curve. The yield stress of 5 MPa in the 100 °C experiment is lower than the yield stress of 10 MPa in the slow and constant volume simulation. After yield, there is a stress plateau followed by a drop in stress that involves melting and, as evidenced in the simulations, significant reconstruction of the crystal domains. The melting starts at a lower strain during the experiment ($e = 0.6$) than the mapped strain predicted from the simulation ($e_m = 1.4$). Additionally, the experimentally observed stress reduction during melting and reconstruction is much lower (~4%) than that calculated by the simulation (~200%). This suggests that the melting and reconstruction are not as pervasive in the experiment, or that they are distributed

over a broader range of strain. Melting is followed by strain hardening, which is less pronounced in the experiment than in the simulations. This is also likely due to the partial melting in the experiment.

Changes in morphology associated with the uniaxial tensile deformation can be assessed by computing the % crystallinity as a function of deformation strain. A comparison of the computed change in % crystallinity from the simulations and from the experimental WAXD patterns is shown in Figure 12.

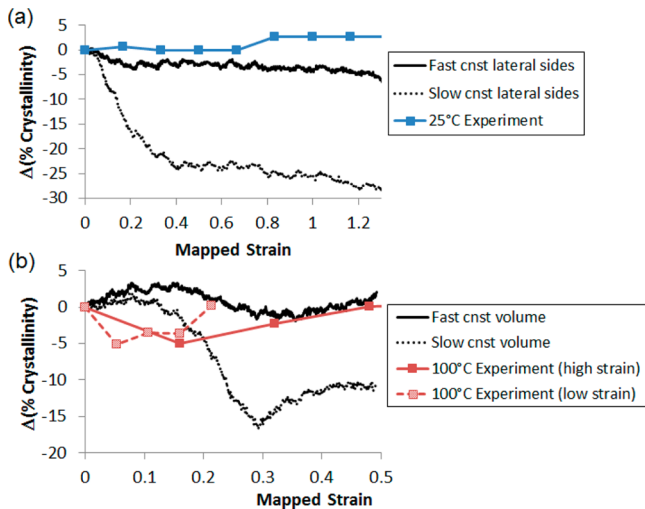


Figure 12. Change in percent crystallinity in simulations of deformation with (a) constant lateral dimensions and the 25 °C experiment, and (b) constant volume simulations and two 100 °C experiments. Two experiments were performed at 100 °C; one with a higher collection frequency deformed to 1.5 strain (dashed red line) and one with a lower collection frequency deformed to 3.0 strain (solid red line).

The crystallinity from the simulations was determined first by computing a local Herman's orientation factor, $P_2(r)$, of each bead, where $r < 0.4$ nm, in three dimensions. Beads are considered crystalline if $P_2(r) > 0.6$. As discussed in ref 16, the choice of order parameter and the cutoff of 0.6 for crystallinity calculations are somewhat arbitrary, and thus, the comparisons of calculated crystallinity changes to those of experimental findings are qualitative.

Experimentally determined crystallinity values during deformation at 25 °C are consistently higher than the values obtained from the simulations with constant lateral dimensions. This is expected since the simulations were conducted at $T = 77$ °C, ensuring more thermal energy and a subsequent lower crystallinity. However, the change in crystallinity during simulated deformation should be comparable to the experimentally measured change in crystallinity. Figure 12 shows that the changes in crystallinity during the simulated deformations depend on both the simulation strain rate and the boundary conditions. Under simulation conditions with fixed lateral sides, the crystallinity stays relatively constant during the fast deformation, but decreases markedly during the slow deformation, as shown in Figure 12a. The crystallinity during the 25 °C deformation experiment remains relatively constant up to $e = 0.7$, although it does increase at higher strains by about 3%. Hence, the 25 °C experiment more closely resembles the fast deformation simulation with constant lateral dimensions. However, the experimentally observed transition

from an orthorhombic crystalline unit cell to a mix of monoclinic and orthorhombic structure at $e = 1.0$ is not observed in the simulation because the UA PE model only exhibits one low energy crystal packing structure. The fast deformation simulation with fixed lateral sides was expected to coincide with the low temperature deformation experiment because both are likely exploring similar configuration space that gives rise to similar deformation mechanisms. At low temperatures where the ground state energy dominates, the crystalline regions would persist upon deformation. Thus, the crystallites could act as a natural barrier to constriction in the lateral dimension. This effectively corresponds to a deformation with constant lateral dimensions in the mechanical unit cell. In addition, the lower temperature experimental system lacks thermal energy required to surmount free energy barriers and to fully explore available conformation space. A similar phenomenon happens in the fast deformation simulation where exploration is restricted because deformation is faster than the average relaxation time of the polymer chains.

The crystallinity during the slow, constant volume simulation and during the 100 °C deformation experiment both exhibit a decrease in crystallinity with strain followed by a reconstruction phase, as shown in Figure 12b. This trend is consistent with the observed similarity in the stress-strain curves in Figure 11b. Both simulation and experimental results show an initial crystallinity near 60% with more melting after yielding indicated from simulations (almost a 30% drop in degree of crystallinity versus the 9% drop observed experimentally). Unlike comparisons with other deformation features, the melting of the crystalline regions occurs at higher strains in the simulation than observed from the experiment. This may be attributed to the “infinite” lamellae resulting from the crystallite periodic boundary conditions imposed in the simulation that would resist melting from the lateral planes. The probability of observing this melting mechanism is thus much lower in the simulations than in the experiment.

The similarity between the high temperature deformation experiment and the slow and constant volume simulation is also consistent with physical interpretation. The crystalline regions during the high temperature deformation could exhibit strain-induced melting and the lateral dimensions of a lamellar stack would then decrease proportional to the increase in the deformation axis. This effectively corresponds to a deformation with constant volume where the lateral dimensions are decreasing with increasing strain in the stretching direction. Additionally, the higher temperature system has enough thermal energy to surmount free energy barriers and to explore more conformation space. The slow deformation simulations allow enough time for the system to similarly explore more conformations. Thus, the high temperature deformation experiment corresponds to the slow deformation simulation with a constant volume.

The evolution of the lamellar morphology with strain was analyzed for the constant volume simulations by considering the Gibbs dividing surface between the crystalline and noncrystalline regions. In this analysis, the mass density profile is computed along the deformation (z -) axis. The transition between crystalline (high mass density) and noncrystalline regions is fit to a step function and the location of the step is the Gibbs dividing surface.²⁹ Unlike the calculation of crystallinity, this procedure is purely based on mass density and does not take into account local chain orientation. Thus, the interfacial region between crystalline and amorphous

regions, where the packing density of united atoms is still high but the chains are not well aligned, are interpreted as crystalline. During deformation where the crystalline region melts, as is the case for the slow and constant volume simulation, this interfacial region will rapidly “melt out” leading to a growth in the amorphous region.

As shown in Figure 13a, the amorphous region grows more than an affine deformation (marked as a red line, representing

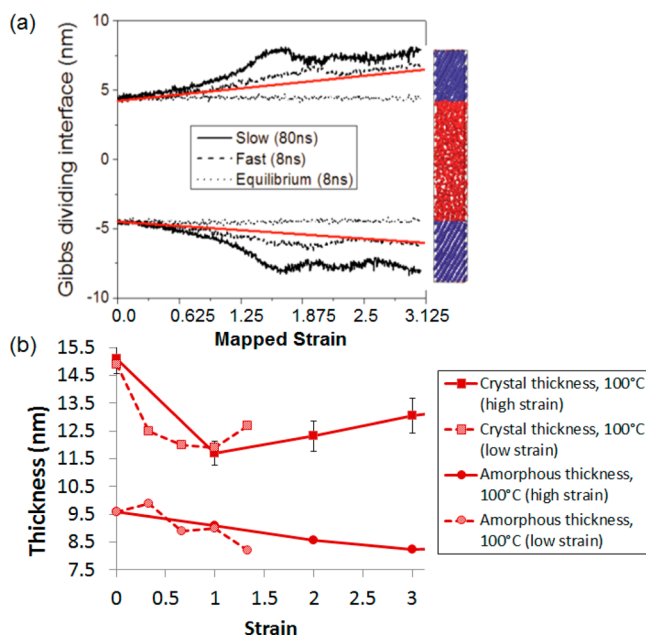


Figure 13. Evolution of lamellar morphology. (a) Gibbs dividing interfaces between crystalline (shown as the two blue regions on the right side of the figure) and noncrystalline domains (shown as the red region on the right side of the figure) as a function of strain for the constant volume “slow” and “fast” deformation simulations. The red line represents a hypothetical affine deformation, and the equilibrium data is from a simulation with no deformation. (b) Crystal (squares) and amorphous (circles) thickness of the HDPE computed from SAXS and WAXD data collected from two experiments during 100 °C uniaxial deformation. As in Figure 12, the two experiments employed different collection frequencies to capture the low strain behavior.

equal strain in crystalline and noncrystalline regions) during the slow and constant volume simulated deformation. This amorphous thickness reaches a maximum around a simulated strain of 0.27, which is the strain at the completion of melting where the stress is minimal in Figure 11b. After a reconstruction period (simulated $e = 0.3$), the amorphous region grows at a rate similar to an affine deformation. This finding implies that the softer, noncrystalline region contributes more to the deformation strain. However, this interpretation is tempered since the Gibbs dividing surface may underestimate the initial number of beads within the noncrystalline region. Because of this reason, it is difficult to compare the crystalline and amorphous thicknesses during the 100 °C experimental deformation, shown in Figure 13b, with the simulation results. The experimental results, mapped onto the simulated strain, show an initial drop in both crystalline and amorphous thicknesses up to $e_m = 0.2$. The long period also decreases during this low strain period, which is likely caused by residual alignment in the strain direction. This residual alignment could cause a drop in amorphous thickness and may explain why it is not observed in the simulations. The drop in crystalline

thickness can be attributed to melting during deformation. At higher strains, the crystalline regions grow by the imposed chain alignment.

CONCLUSIONS

The controlled in situ SAXS/WAXD deformation experiment on a uniaxially oriented PE fiber provides a system to directly compare to the plastic deformation simulation results of a semicrystalline lamellar model. This comparison provides bounds in which to interpret further simulation results. In general, discernible features in the simulated stress-strain curves happen with higher and more pronounced changes in stress, and at lower strains as a consequence of the united atom model used for PE and the periodic boundary conditions imposed. Also, the simulations average over only 18 different structures, all of which are perfectly aligned. Thus, the changes in simulated stress occur at similar strains and tend to be abrupt. Nonetheless, simulations were shown to be able to capture a full range of observed experimental behavior by varying deformation rate and boundary conditions. The correspondence of rate with experimental temperature is simply a time–temperature superposition. The dependence on the simulation boundary conditions highlights the different observed experimental deformation mechanisms—crystallographic slip and strain-induced melting. One could likely find similar deformation mechanisms by varying the simulation temperature rather than the boundary conditions. With these performance boundaries in mind, one can now devise systematic studies using this SM model in order to understand how amorphous topology affects plastic deformation and the stress within the system.

AUTHOR INFORMATION

Corresponding Author

*E-mail: (J.C.) justinche1@gmail.com.

Notes

The authors declare no competing financial interest.

REFERENCES

- (1) Kolgjini, B.; Schoukens, G.; Kiekens, P. *Int. J. Polym. Sci.* **2011**, 731708, 1–7.
- (2) Na, B.; Zhang, Q.; Fu, Q.; Men, Y.; Hong, K.; Strobl, G. *Macromolecules* **2006**, 39, 2584–2591.
- (3) Fu, Q.; Men, Y.; Strobl, G. *Polymer* **2003**, 44, 1927–1933.
- (4) Hobeika, S.; Men, Y.; Strobl, G. *Macromolecules* **2000**, 33, 1827–1833.
- (5) Stribeck, N.; Alamo, R. G.; Mandelkern, L.; Zachmann, H. G. *Macromolecules* **1995**, 28, 5029–5036.
- (6) Fu, Q.; Men, Y.; Strobl, G. *Polymer* **2003**, 44, 1941–1947.
- (7) Jiang, Z.; Tang, Y.; Men, Y.; Enderle, H.; Lilge, D.; Roth, S. V.; Gehrke, R.; Rieger, J. *Macromolecules* **2007**, 40, 7263–7269.
- (8) Tang, Y.; Jiang, Z.; Men, Y.; An, L.; Enderle, H.; Lilge, D.; Roth, S. V.; Gehrke, R.; Rieger, J. *Polymer* **2007**, 48, 5125–5132.
- (9) Uribe, A.; Manzur, A.; Olayo, R. *J. Mater. Res.* **2012**, 27, 1351–1359.
- (10) Bowden, P. B.; Young, R. *J. Mater. Sci.* **1974**, 9, 2034–2051.
- (11) Goderis, B.; Reynaers, H.; Koch, M. H. J.; Mathot, V. B. F. *J. Polym. Sci., Part B: Polym. Phys.* **1999**, 37, 1715–1738.
- (12) Hiss, R.; Hobeika, S.; Lynn, C.; Strobl, G. *J. Macromol. Sci., Part B: Phys.* **1999**, 38, 847–858.
- (13) Hiss, R.; Hobeika, S.; Lynn, C.; Strobl, G. *Macromolecules* **1999**, 32, 4390–4403.
- (14) Moysés, S. C.; Machado, R. *Eur. Polym. J.* **2002**, 38, 2041–2044.
- (15) Hong, K.; Strobl, G. *Macromolecules* **2006**, 39, 268–273.
- (16) Lee, S.; Rutledge, G. C. *Macromolecules* **2011**, 44, 3096–3108.

- (17) Veld, P. in't; Rutledge, G. C. *Macromolecules* **2003**, *36*, 7358–7365.
- (18) Humbert, S.; Lame, O.; Chenal, J.; Rochas, C.; Vigier, G. *J. Polym. Sci., Part B: Polym. Phys.* **2010**, *48*, 1535–1542.
- (19) Wilchinsky, Z. *J. Appl. Phys.* **1960**, *31*, 1969–1972.
- (20) Desper, C.; Stein, R. *J. Appl. Phys.* **1966**, *37*, 3990–4002.
- (21) Hermans, J. *J. Recl. Trav. Chim. Pays-Bas* **1944**, *63*, 211–218.
- (22) Stribeck, N. *Macromolecules* **1996**, *29*, 7217–7220.
- (23) Ruland, W.; Smarsly, B. *J. Appl. Crystallogr.* **2004**, *37*, 575–584.
- (24) Burger, C.; Zhou, H.; Wang, H.; Sics, I.; Hsiao, B. S.; Chu, B.; Graham, L.; Glimcher, M. *J. Biophys. J.* **2008**, *95*, 1985–1992.
- (25) in 't Veld, P. J.; Hutter, M.; Rutledge, G. C. *Macromolecules* **2006**, *39*, 439–447.
- (26) Eyring, H. *J. Chem. Phys.* **1936**, *4*, 283–291.
- (27) Sweeney, J.; Shirataki, H.; Unwin, A. P.; Ward, I. M. *J. App. Polym. Sci.* **1999**, *74*, 3331–3341.
- (28) Capaldi, F. M.; Boyce, M. C.; Rutledge, G. *Polymer* **2004**, *45*, 1391–1399.
- (29) Hutter, M.; Veld, P. in't; Rutledge, G. C. *Polymer* **2006**, *47*, 5494–5504.